JWST's first view of the most vigorously star-forming cloud in the Galactic center – Sagittarius B2

Nazar Budaiev [ID],[1] Adam Ginsburg [ID],[1] Ashley T. Barnes [ID],[2] Desmond Jeff [ID],[1] Taehwa Yoo [ID],[1] Cara Battersby [ID],[3] Alyssa Bulatek [ID],[1] Xing Lu [ID],[4, 5] Elisabeth A.C. Mills [ID],[6] and Daniel L. Walker [ID][7]

[1]*Department of Astronomy, University of Florida, P.O. Box 112055, Gainesville, FL 32611, USA*
[2]*European Southern Observatory (ESO), Karl-Schwarzschild-Straße 2, 85748 Garching, Germany*
[3]*Department of Physics, University of Connecticut, 196A Auditorium Road, Unit 3046, Storrs, CT 06269, USA*
[4]*Shanghai Astronomical Observatory, Chinese Academy of Sciences, 80 Nandan Road, Shanghai 200030, P. R. China*
[5]*State Key Laboratory of Radio Astronomy and Technology, A20 Datun Road, Chaoyang District, Beijing, 100101, P. R. China*
[6]*Department of Physics and Astronomy, University of Kansas, 1251 Wescoe Hall Drive, Lawrence, KS 66045, USA*
[7]*UK ALMA Regional Centre Node, Jodrell Bank Centre for Astrophysics, The University of Manchester, Manchester M13 9PL, UK*

ABSTRACT

We report JWST NIRCAM and MIRI observations of Sgr B2, the most active site of star formation in the Galaxy. These observations, using 14 filters spanning 1.5 to 25 microns, have revealed a multilayered and highly structured cloud that contains both a revealed, low-extinction and hidden, high-extinction population of massive stars. JWST has detected new candidate H II regions around massive stars previously missed by radio telescopes. MIRI has detected radiation escaping from the forming massive cluster Sgr B2 N along its outflow cavities, demonstrating that infrared radiation finds geometric escape routes even in the densest, most heavily embedded regions in the universe. JWST further highlights the gas asymmetry in the cloud, showing a sharp, straight cutoff along the eastern cloud edge.

Despite the great sensitivity of these observations, no extended population of YSOs has been detected, placing a limit on their minimum extinction; this result hints that star formation has only just begun in the cloud. Together, these results suggest that, despite already holding the crown for most actively star-forming cloud, we have underestimated the total star formation in Sgr B2. JWST unveils previously hidden massive stars and ionized structures, offering a transformative view of how stars form under some of the most extreme Galactic conditions.

1. INTRODUCTION

Stars form differently in star clusters, with probable differences in the initial mass function (IMF, e.g., M. W. Hosek et al. 2019), multiplicity (G. Duchêne et al. 2018), and planets (P. J. Armitage 2000; E. C. Daffern-Powell & R. J. Parker 2022). Such clusters represent a large fraction, in some cases even the majority, of star formation in the earliest galaxies (e.g. J. M. D. Kruijssen 2012; J. M. D. Kruijssen & S. N. Longmore 2013; J. Pfeffer et al. 2018). The Central Molecular Zone (CMZ) of our Galaxy is an excellent local laboratory in which to study massive cluster formation. The CMZ hosts such embedded and forming clusters (A. Schmiedeke et al. 2016) and has gas conditions similar to those in high-redshift star-forming galaxies (J. D. Henshaw et al. 2022; J. M. D. Kruijssen & S. N. Longmore 2013). These gas conditions drive differences in the star formation process. In particular, the high-pressure environment of the CMZ leads

stars forming in dense, warm, and turbulent molecular clouds to do so preferentially in dense, massive clusters (A. Ginsburg & J. M. D. Kruijssen 2018; D. L. Walker et al. 2016).

Despite containing around 80 percent of the Galaxy's dense molecular gas, the CMZ only forms around 10 percent of the Galaxy's stars, more than an order of magnitude lower from what we expect according to the typical dense gas relations (A. T. Barnes et al. 2017; S. N. Longmore et al. 2013). Investigating and characterizing the star-forming population within the extreme environment of the CMZ is crucial to understand the low star formation rate and to evaluate the assumptions used for stellar populations within extragalactic Super Star Clusters (SSCs).

Sagittarius B2 (Sgr B2), is a powerful laboratory for studying star formation and evolution in conditions similar to the most active period of cosmic star formation (z ≈ 2) (P. Madau & M. Dickinson 2014). The molecular cloud is situated ∼100 pc away in projection from the Galactic center, located 8.277 kpc away (GRAVITY
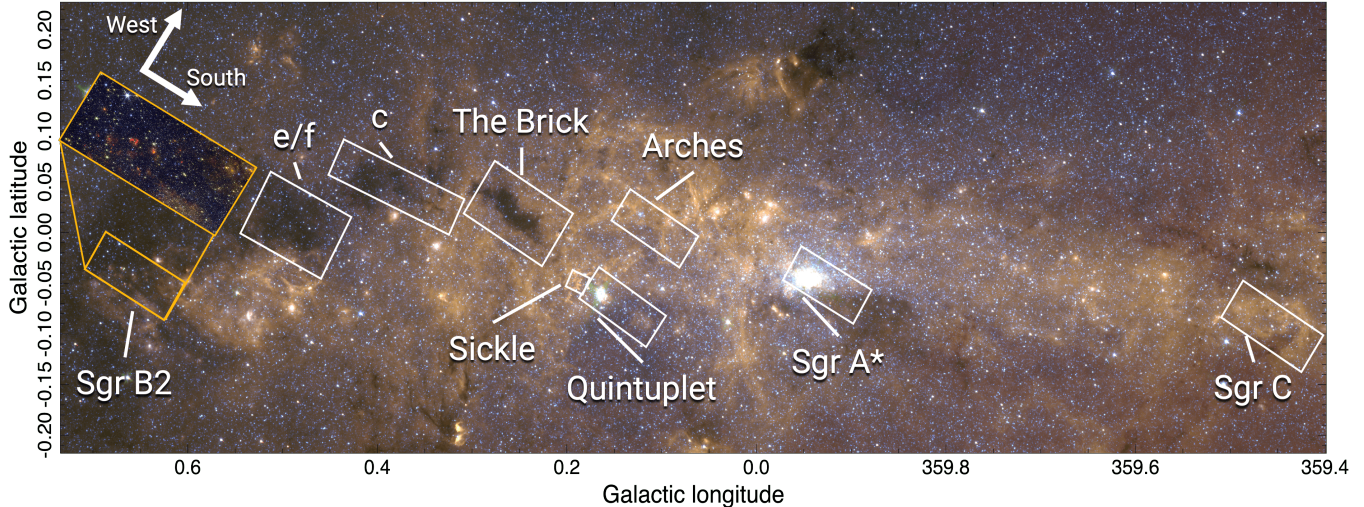
Email: nbudaiev@ufl.edu

Figure 1. The overview of the CMZ with a *Spitzer* IRAC tricolor image. The footprints of the currently completed JWST programs in the CMZ are shown with white rectangles. These include observations of molecular clouds Sgr B2 (this work, PID: 5365), cloud e/f (PID: 2092), cloud c (PID: 2221), The Brick (PIDs: 1182, 2221 (A. Ginsburg et al. 2023), 2526, 6927), and Sgr C (PID: 4147 (S. Crowe et al. 2025)), star clusters Arches (PID: 2045) and Quintuplet (PID: 2045), as well as Sickle region (PID: 3958) and Sgr A*/nuclear star cluster (PIDs: 1939, 3571, 5368, 6095). The relative orientation of the top panel of Figure 2 is shown with a yellow rectangle. An interactive view of the JWST observations of the Galactic center can be viewed at: https://starformation.astro.ufl.edu/avm_images/jwst_cmz_hips.

Collaboration et al. 2022). Sgr B2 is forming stars at a rate of 0.04 $M_\odot$ yr^{-1}, almost half of all the star formation in the CMZ, and thus is one of the most star-forming clouds in our Galaxy (A. Ginsburg et al. 2018). Interferometry with long baselines has enabled resolved studies of the star-forming populations in the cloud; the cloud contains over 700 YSOs, over 50 H II regions, many outflows, dozens of hot cores, and hundreds of masers (A. Ginsburg et al. 2018; N. Budaiev et al. 2024; A. Schmiedeke et al. 2016; F. Meng et al. 2022; D. Jeff et al. 2024; N. Budaiev et al. 2025). JWST's sensitivity and resolution allows us to probe recent, but less embedded, star formation on similar scales.

We present the first findings of the JWST NIRCam and MIRI observations of Sgr B2. In Section 2 we describe the observational setup and data reduction procedures. Section 3 explains the creation of an extinction map and SED fitting. In Section 4 we present new and unanticipated findings and discuss the implications with the conclusions summarized in Section 5.

2. OBSERVATIONS AND DATA REDUCTION

JWST observed the extended Sgr B2 cloud as a part of program 5365 (PIs: A. Ginsburg, N. Budaiev). The data presented in this paper were obtained from the Mikulski Archive for Space Telescopes (MAST) at the Space Telescope Science Institute (STScI). NIRCam observations were completed on September 7th 2024. MIRI observations were split into two visits: the northern part of the cloud was observed on September 15th 2024, and the remaining half was observed on September 2nd 2025.

The observations include 11 NIRCam filters and 3 MIRI filters. The majority of the NIRCam filters used the SHALLOW2 readout pattern with three groups per integration to reduce saturation in the bright stars; the filter pair with the longest exposure, F187N and F405N, used the MEDIUM8 readout pattern to reduce the data rate. The observations were ordered by increasing filter bandwidth and from shortest to longest wavelength to mitigate persistence. The MIRI observations did not include a background pointing. Due to broad and bright emission throughout the CMZ, there is not a suitable location to measure true background. The details of the observational setup are presented in Tables 1 and 2.

2.1. *Imaging*

We imaged the data using STScI's science calibration pipeline version 1.15.1. The NIRCam imaging was done with `suppress_one_group=False` to recover some of the saturated areas. An overview tricolor image is shown in the top panel of Figure 2. The MIRI data, especially in the F2550W filter, are saturated around the bright H II regions. Thus, MIRI data were imaged twice: once for source cataloging and once for image presentation. The version for the source cataloging used the standard pipeline parameters with an addition of sky subtraction with `skymatch` set to `match`. We imaged the data again with all saturation flagging turned off. These latter images are used purely for better visual presentation of

Table 1. Observation setup for NIRCam.

Short Filter	Long Filter	Readout	Groups/Int	Int/Exp	Dithers	Integrations	Exposure Time
F212N	F466N+F444W	SHALLOW2	3	1	24	24	3092 s
F187N	F405N+F444W	MEDIUM8	4	1	24	24	9792 s
F187N	F300M	SHALLOW2	3	1	24	24	3092 s
F210M	F480M	SHALLOW2	3	1	24	24	3092 s
F182M	F410M	SHALLOW2	3	1	24	24	3092 s
F150W	F360M	SHALLOW2	3	1	24	24	3092 s

Table 2. Observation setup for MIRI.

Filter	Readout	Groups/Int	Int/Exp	Exp/Dith	Dither	Dithers	Ints	Exp Time
F770W	FASTR1	8	2	1	Cycling large	5	10	235.878 s
F1280W	FASTR1	8	2	1	Cycling large	5	10	235.878 s
F2550W	FASTR1	8	2	1	Cycling large	5	10	235.878 s

the figures in this work. The MIRI tricolor image is presented in bottom panel of Figure 2.

All figures in this work are plotted with Declination on the x-axis following the default JWST file orientation. Figure 3 shows the cardinal directions relative to the JWST footprint as well as the main features of the cloud.

2.2. *Source extraction*

The source extraction for NIRCam filters is performed following the methods described in A. Ginsburg et al. (2023) (see their Sections 3.3 and 3.4). In summary, `crowdsource` in combination with `webbpsf` and `stpsf` (M. D. Perrin et al. 2012, 2014) are used on the individual calibrated exposures to produce a catalog for each frame, which are subsequently merged. The catalog for each filter are then combined by cross-matching detections and excluding any matches with a separation of $d > 0.''1$. We then filter the catalog by "quality factor" `qf`> 0.75, how extended the source is `spread` < 0.25, magnitude error `emag` < 0.1, and fraction of flux attributed to the source's PSF `fracflux`> 0.8. There are 1,293,208 sources with a good measurement in at least one of the filters, 84,490 sources with a good measurement in all of the filters where the source was detected, and 29,006 sources with a good measurement in all eleven filters.

We utilize the STScI's pipeline implementation of `DAOphot` to extract sources in the three MIRI filters. We set the `kernel_fwhm` parameter to the PSF's FWHM in pixels for each filter. Since observing a dedicated background field is not feasible for a Galactic center target, the true background level is uncertain. The imaging utilizes the `skymatch` method set to `match`, matching down. This strategy allows for smooth background matching between the frames without making assumptions about the large-scale background. The background-subtracted aperture photometry performed on point-sources is sufficient to exclude any large-scale background contribution.

The MIRI images contain a lot of smaller-scale extended but structured emission. We choose `bkg_boxsize` of 60 pixels for F2550W, 35 pixels for F1280W, and 25 pixels F770W to improve the source extraction in the regions close to the bright extended emission. We then exclude any detection with `is_extended` flag, resulting in 3726 detections at $7.7\,\mu$m, 1612 detections at $12.8\,\mu$m, and 209 detections at $25.5\,\mu$m. We note that, while the `daophot`'s `is_extended` classification performs well at the shorter wavelengths, more than half of sources classified as point sources in F2550W are instead extended. This brings down the number of true point sources to about 50, not including some of the faint objects missed by the cataloging tool. Finally, the F2550W filter observations are affected by persistence from the preceding observations with F1280W filter (see Appendix A).

After performing by-eye inspection and preliminary analysis of the catalogs described in Section 4.7, it is evident that, while these catalogs are sufficient to identify the general features of the observed populations,
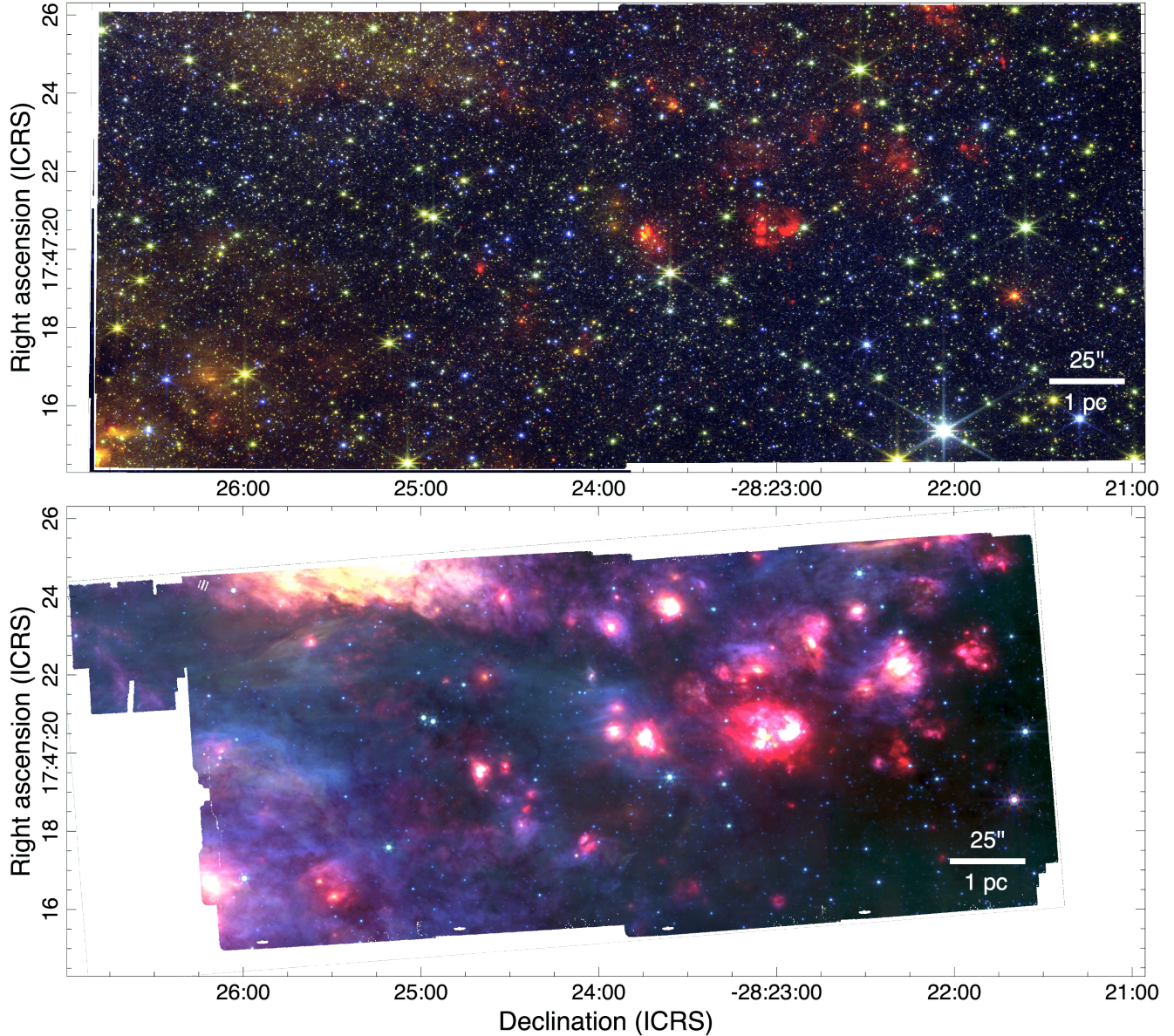
Figure 2. Top: NIRCam mosaic of Sgr B2 with F480M in red, F360M in green, and F150W in blue. Bottom: MIRI mosaic of Sgr B2 with F2550W in red, F1280W in green, and F770W in blue. This and all other figures in this work have Declination on the x-axis.

a more sophisticated approach is needed to isolate the sparser populations (e.g. YSOs, UCH II regions). We subjectively rank the main factors impacting the catalog uncertainty, from most to least important: source density, extended psf artifacts, and extended emission for NIRCam. MIRI catalogs are primarily affected by the structured extended emission. An in-depth performance analysis of cataloging tools as well as source extraction uncertainty mitigation will be performed elsewhere.

2.3. *Other data*

In this work, we compare the JWST data to ALMA observations from N. Budaiev et al. (2024), A. Ginsburg et al. (2018), and 2017.1.00114.S, MeerKAT data from I. Heywood et al. (2022), and VLA data from F. Meng et al. (2019) and N. Budaiev et al. (2025).

3. ANALYSIS

3.1. *Recombination line extinction map*

Extinction is wavelength dependent; thus, the intrinsic ratio of the emissivities of recombination lines can be used to derive the extinction. Emissivity is defined as
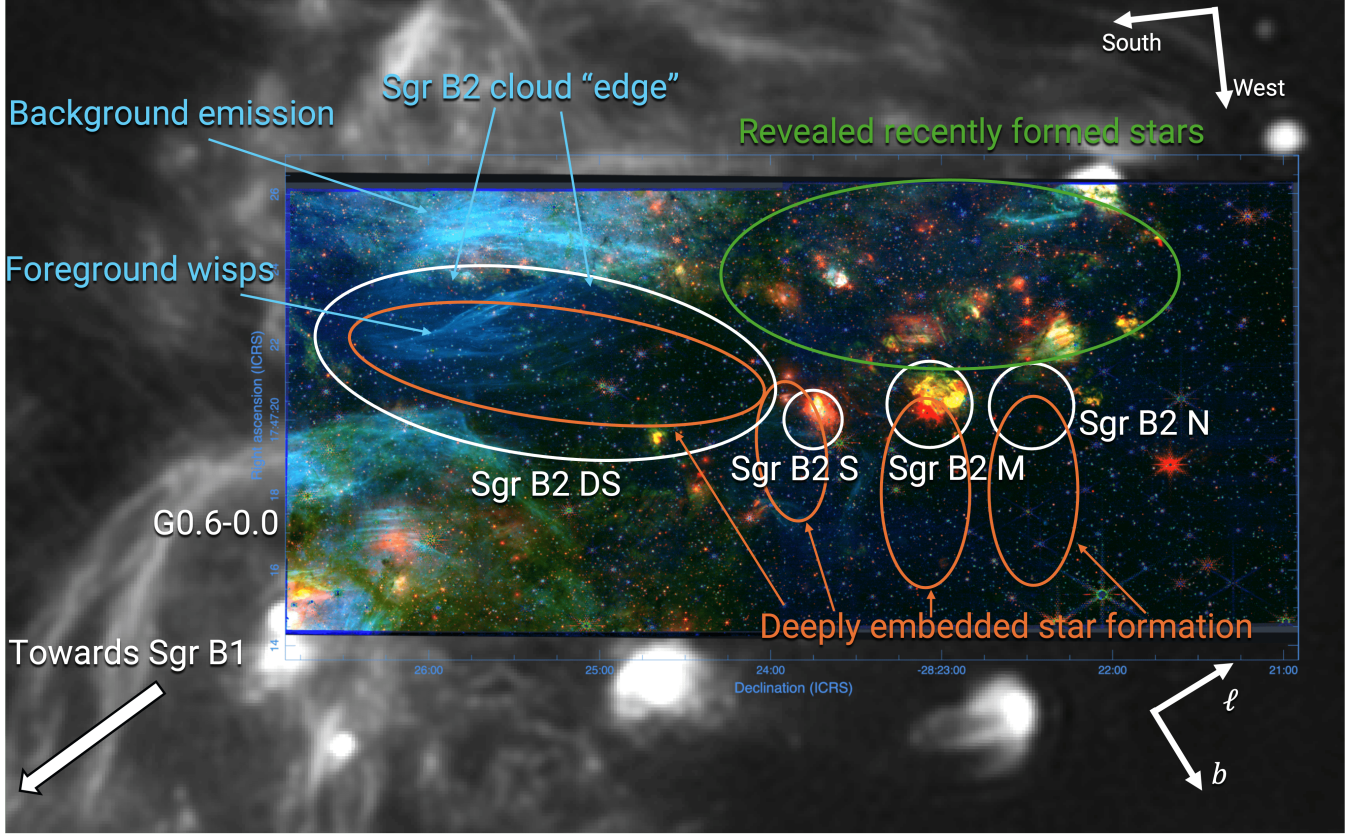
$$j_\nu \equiv \frac{dI_\nu}{ds}, \tag{1}$$

Figure 3. A NIRCam tricolor figure overlaid on top of MeerKAT 1.2 GHz continuum with the main parts of the cloud and the observed features labeled. Red is F480M−F360M, green is Brα, and blue is Paα. The blue color represents low extinction, green shows regions with higher extinction, and red shows warm dust.

where I_ν is the surface brightness. If the emission is optically thin, then the path length of Paα and Brα is the same, and thus

$$\frac{I_{\mathrm{Pa\alpha}}}{I_{\mathrm{Br\alpha}}} = \frac{j_{\mathrm{Pa\alpha}}}{j_{\mathrm{Br\alpha}}}. \qquad (2)$$

The pipeline-delivered data are in MJy sr^{-1}, so in order to compare the line surface brightness in different filters, we need to account for the bandwidth difference. Assuming no extinction, the ratios of observed bandwidth-scaled lines and emissivities should be the same:

$$\frac{I_{F187N} \times BW_{F187N}}{I_{F405N} \times BW_{F405N}} = \frac{j_{\mathrm{Pa\alpha}}}{j_{\mathrm{Br\alpha}}} = R, \qquad (3)$$

where I_{filter} is the observed surface brightness in the given filter, and BW_{filter} is the bandwidth of the filter. At T=10^4 K, $\frac{j_{\mathrm{Pa\alpha}}}{j_{\mathrm{Br\alpha}}} = 4.24$ (B. T. Draine 2011).

Let $k_\lambda = \frac{A_\lambda}{A_V}$, where k is the assumed extinction curve. Then the extinction is:

$$A_V = \frac{2.5 \log_{10}(R_0/R_{obs})}{(k_{\lambda_1} - k_{\lambda_2})}, \qquad (4)$$

where R_{obs} is the observed ratio, R_0 is the intrinsic ratio.

We produce continuum-subtracted recombination line images by first subtracting the line contribution from the corresponding continuum filter image and then subtracting the resulting line-free continuum image from the narrow-band data. We refer the reader to the Section 3.5 of A. Ginsburg et al. (2023) for the detailed explanation of the continuum-subtracted line image creation.

We assume an extinction law from J. E. Chiar & A. G. G. M. Tielens (2006)[8] to compute the A_V over the whole FOV. This extinction law is chosen as it is suitable for the Galactic center and covers all of the observed filters. Then, we visually inspect the Paα and Brα images to identify the minimum flux where the extended emission can be distinguished from the background 1/f noise: 1.5 MJy sr^{-1} for Paα and 3 MJy sr^{-1} for Brα. We create two maps using these emission thresholds as masks: the Paα-based map is constrained to regions that have emission in both lines, while the Brα-based map includes regions that do not have Paα emission present, but do have the Brα emission visible. The regions with only

---

[8] `CT06-MWGC` extinction curve in `dust_extinction` package.

Brα emission are still useful as they set a lower limit on the extinction.

The resulting images contain visual artifacts from the bright stars; the short- and medium-band filters have significantly different PSFs and thus the continuum-subtracted images contain characteristic spikes. The different size of the PSF prevents a proper subtraction of faint stars, as well, resulting in small, isolated groups of pixels with non-physical extinction values. We remove the diffraction artifacts and the isolated stars from the extinction maps by removing isolated groups of pixels via `remove_small_objects` from `scipy.morphology`. We set the minimum size at 30 and 250 pixels for Paα- and Brα-based maps respectively. In addition, 1/f noise in the shorter wavelength images results in faint horizontal striping in the resulting extinction map, primarily on the left side of the image.

The Brα-based extinction map is shown in Figure 4. The black contours enclose the regions where both Paα and Brα recombination lines are detected; any point outside the contours is only detected in Brα and thus is a lower limit on the extinction. In such cases, we still use the pixel values from the Paα map instead of a constant value to compute the lower limit on extinction. This choice results in a visually smoother map. This measurement will be discussed further in Section 4.1.

3.2. *SED of an* H II *region*

We construct the SEDs of several known HCH II regions that are detected with VLA, ALMA, and now JWST. We highlight the SED of UCH II region X8.33 in Figure 5 as it is the easiest to interpret: it is isolated, resolved in one of the observations, and detected in the greatest number of JWST filters. As shown in Fig 5, this HII region is best fit by a free-free model at most wavelengths, with a contribution from warm dust in MIRI filters and stellar emission in NIRCam filters, behind a screen of $A_V \gtrsim 180$.

The X8.33 H II region is located west of Sgr B2 N, next to ALMA-detected YSOs (see Figures 7 and 10). The long-baseline 3 mm data spatially resolves the source to have $r = 1500$ au (0.014 pc). Using the 6 and 22 GHz data from F. Meng et al. (2022) and the 92 GHz data from N. Budaiev et al. (2024), we determine the spectral index in the radio regime: ∼0.15 between 92 and 22 GHz and ∼0.25 between 22 and 6 GHz. The low spectral index suggests that the H II region is dominated by free-free emission and is optically thin at 22 GHz. Thus, we extrapolate the emission from 22 GHz into the infrared assuming $S_\nu \propto \nu^{-0.1}$. The extrapolated emission should hold until $h\nu \gtrsim kT_e$, which, assuming $T_e \sim 10^4$

K, should be valid until ∼1.5 µm (G. B. Rybicki & A. P. Lightman 1979).

At 92 GHz, the extrapolated free-free emission is consistent with the observed flux.

F. Meng et al. (2022) reported the spectral type of the central star of B0 based on the rate of ionizing photons $\log_{10}\left(\dot{N}_{\mathrm{Ly}}/\mathrm{s}^{-1}\right) \approx 46.6$. We incorporate stellar emission in the SED using a blackbody model with $T = 30,000$ and $r = 7.4\,\mathrm{R}_\odot$. From here, we assume that at 4 µm the free-free and stellar emission dominate over the dust emission to estimate the lower limit on the extinction. Using the J. E. Chiar & A. G. G. M. Tielens (2006) extinction law, we estimate that a minimum of $A_V \gtrsim 140$ is required to explain the observed flux at 4 µm. If the dust emission dominates, the extinction would have to be even higher. The significant excess emission observed above 4.8 µm indicates the presence of hot dust that dominates at mid-infrared wavelengths.

At 4 µm, blackbody radiation from the dust dominates at $T \geq 190$ K assuming that the emitting dust has the same physical extent as the free-free emission seen at 92 GHz or $r = 1500$ au. An even higher temperature is required to explain the high flux observed in the F2550W filter. The high observed MIRI fluxes imply that dust is a minor contributor to the 92 GHz flux. Figure 5 shows that the observed SED is somewhat consistent with $T_d = 200$ K, $A_V = 180$ assuming an extinction curve from J. E. Chiar & A. G. G. M. Tielens (2006). However, due to the uncertainty on the true shape of the extinction curve (F. Nogueras-Lara et al. 2019) and a lack of direct temperature measurements, these are likely only rough estimates. At the same time, the $A_V \sim 200$ aligns with extinction estimates based on the surface density reported in A. Ginsburg et al. (2018).

4. DISCUSSION

4.1. *Extinction*

In Section 3.1, we created an extinction map of Sgr B2 using the recombination line ratio. By comparing the extinction map with the existing mm and cm maps (e.g. A. Ginsburg et al. 2018; I. Heywood et al. 2022; F. Meng et al. 2022), we find that the majority of the cloud seen with ALMA and VLA is extremely embedded behind a thick screen of $A_V > 130$. The absence of measurements in the extinction map imply either an extinction $A_V > 130$ or that no extended recombination line emission is present. There are several regions in the cloud where extended radio emission is seen, but no extinction is measured. For example, F. Meng et al. (2019) reports extended free-free emission in Sgr B2 DS. The corresponding region in the extinction map in Figure 4 appears to have very low extinction. Based on the
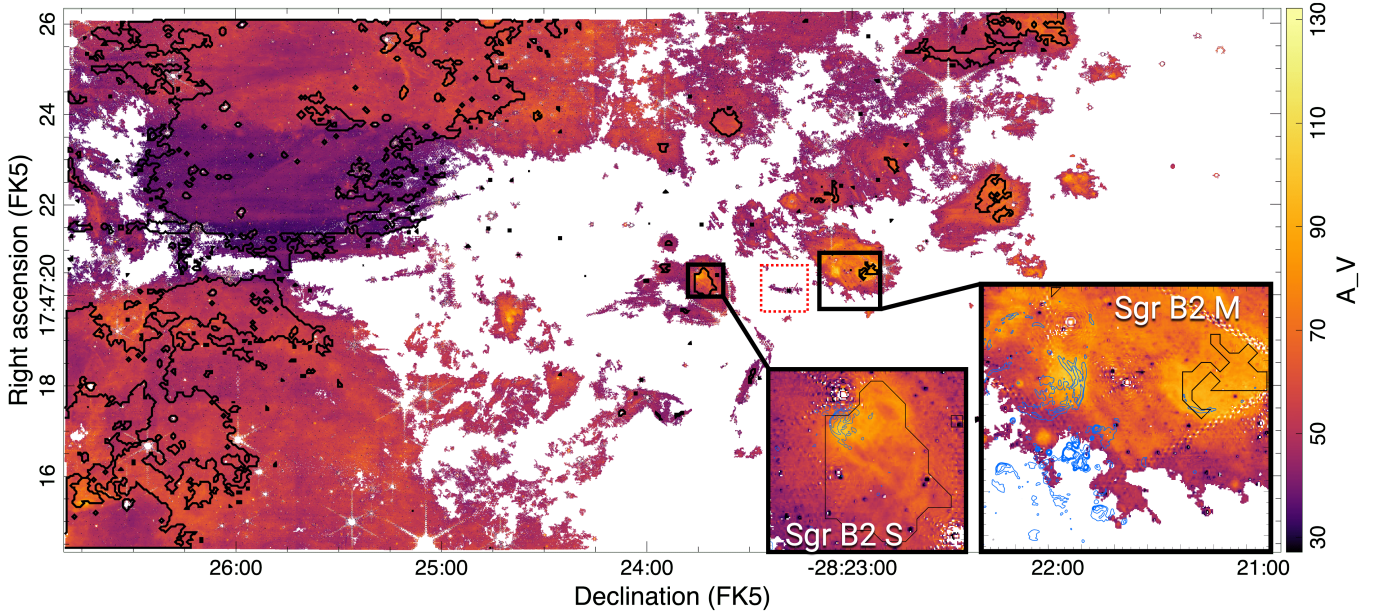
Figure 4. Extinction map based on the Paα and Brα line ratio. The black contours define the areas where both Brα and Paα emission is present. Outside of the black contours, only Brα emission is detected, setting a lower limit on extinction. The apparent dark patch of the map on the left side of the image is coincident with Sgr B2 DS, a region with high column density. The measured extinction is towards a foreground feature; the Sgr B2 DS region is extremely deeply embedded such that ionized material behind it is it not detected in either Paα or Brα. The insets highlight the locations where the extinction is measured towards parts of Sgr B2 M and S, with blue contours from 3 mm data (N. Budaiev et al. 2024). The red dotted square marks the location of one of the few features with an H_2 detection.

morphology of the features in the two data sets, they are likely to be distinct, with the JWST-observed wisps existing in the foreground of Sgr B2 DS.

The rapid change in the observed extinction in the upper left part of the map suggests that the background extended emission located at the very top of the image becomes completely extincted by the dense cloud. As mentioned above, the apparent lower extinction is the product of foreground emission on top of the star-forming ridge Sgr B2 DS. This feature is discussed further in Section 4.6.2.

Only a small fraction of ALMA- and VLA-detected parts of the cloud have an extinction measurement in JWST data. The insets in Figure 4 show the regions with the largest overlap with ALMA 3 mm continuum shown in blue contours: Sgr B2 S is seen at $A_V = 90$, and several H II regions associated with Sgr B2 M are observed at $A_V = 100$. However, the bulk of the Sgr B2 M protocluster is completely extincted in both recombination lines, as is Sgr B2 N. The measured extinction to S and M indicates that these protoclusters began removing the surrounding dust through feedback, whereas Sgr B2 N is still deeply embedded. Typically, due to the large number of H II regions, Sgr B2 M is considered the oldest star forming region in the cloud, followed by Sgr B2 N, and then Sgr B2 S. An alternative interpretation for the observed extinction is that Sgr B2 S is located

closer to the "surface" of the cloud compared to Sgr B2 N.

Dense star forming regions contain a large amount of shocked gas, either from protostellar outflows colliding with the surrounding interstellar medium, or at sites of the cloud-cloud collisions. Many outflows are detected in Sgr B2 DS based on SiO emission (F. Meng et al. 2022), a known shock tracer. Another shock tracer covered with the NIRCam observations is H_2. However, due to high extinction we see no H_2 emission associated with the cloud. One linear feature is detected between Sgr B2 S and M, marked with a red dotted square in Figure 4. A part of this feature is seen in Brα with a lower limit $A_V = 40$.

We adopt an $A_V = 17$ foreground extinction in line with the F. Nogueras-Lara et al. (2021) measurement. A. Ginsburg et al. (in preparation) used the presence of CO ice to estimate the extinction towards a nearby molecular cloud, The Brick, of $A_V = 17$. Our preliminary analysis of the H_2O ice discussed in Section 4.7 matches these results. However, the exact extinction law towards the Galactic Center is uncertain. Using an extinction law from K. D. Gordon et al. (2023) with $R_V = 3.1$ results in an increase in the observed extinction by $\sim 30\%$.
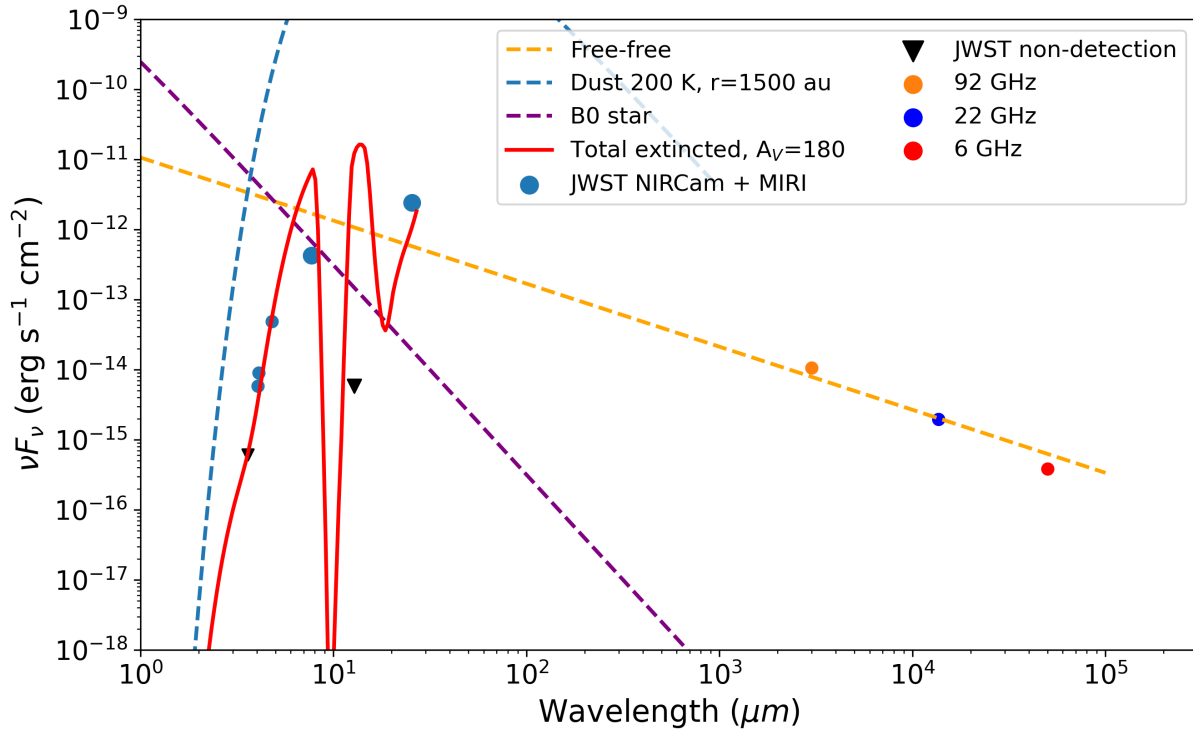
Figure 5. An SED of the X8.33 UCH II region. The contribution of the free-free emission is set by the observations in the radio regime. We estimate the lower-limit on the extinction in the infrared by assuming that free-free emission dominates in the micron range and utilizing the extinction curve from J. E. Chiar & A. G. G. M. Tielens (2006). The stellar type of the central star, and thus the stellar contribution, is derived from the estimates of the number of ionizing photons from F. Meng et al. (2022). The dust contribution is modeled as a blackbody based on the observed size in the 3 mm observations. The remaining free parameters T_d and A_V are fit to match the observed SED. The JWST filter bandwidths are smaller than the marker sizes. The flux error bars are similar to the marker sizes.

4.2. *MIRI reveals radiation escaping Sgr B2 N*

As seen in Figure 6, there is extended $25\,\mu$m emission present surrounding the heart of the Sgr B2 N cluster. This extended emission is detected at $25\,\mu$m only and has no radio counterparts between $1\,$GHz and $230\,$GHz. However, it matches the extent and orientation of the large-scale SiO outflow (A. E. Higuchi et al. 2015; N. Budaiev et al. 2025). This emission is present in *Spitzer* observations, however it is blended with the emission from the surrounding H II regions.

The observed configuration suggests that infrared radiation escaping from the heart of the protocluster is the source of the emission. The radiation is escaping via the lower density regions created by the large-scale outflow. This shows that even in the densest region of our Galaxy, infrared radiation may find a way to escape instead of being trapped inside and repeatedly scattered(T. A. Thompson et al. 2005; M. R. Krumholz & C. D. Matzner 2009; N. Murray et al. 2010; S. H. Menon et al. 2022, 2023). Future MIRI spectroscopic observa-

tions of this emission have the potential to test the theory that these early-stage, mass-regulating outflows are driven by UV radiation at the extreme column densities of super star clusters (Σ(Sgr B2 N) $\gtrsim 10^4\,\mathrm{M_\odot pc^{-2}}$ on parsec scales, S. H. Menon et al. 2023).

4.3. H II *regions*

The extended Sgr B2 cloud hosts a large number of H II regions with scales ranging from 0.005 pc to 1 pc (F. Meng et al. 2022). Our JWST observations are sensitive to two components of the emission from H II regions: recombination line emission and thermal emission from hot dust. The H II regions heat the surrounding gas and dust, resulting a "glow" seen in MIRI and the long-wavelength NIRCam filters. We use the presence of recombination line emission in combination with the extended "glow" to identify new H II region candidates and compare these detections with the existing catalogs of H II regions (e.g. A. Schmiedeke et al. 2016; F. Meng et al. 2022) The spatial distribution of the H II regions is shown in Figure 7.
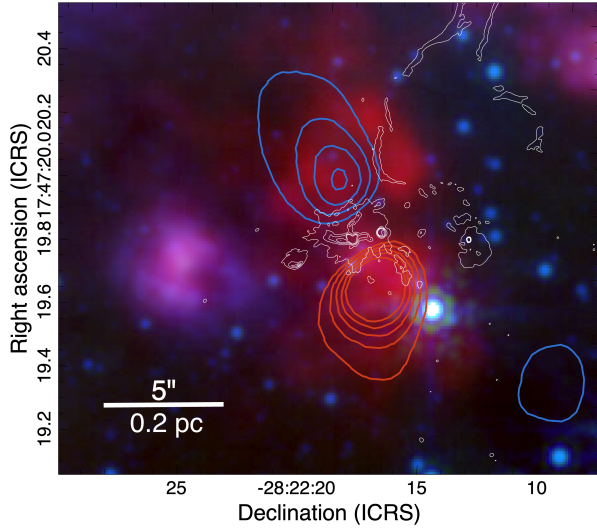
(a) MIRI tricolor image: red is F2500W, green is F1280W, and blue is F770W. The 3 mm continuum emission from panel (b) is shown as white contours. The red and blue contours show the integrated intensity map of SiO emission between 5 and $55\,\mathrm{km\,s^{-1}}$ and 85 and $115\,\mathrm{km\,s^{-1}}$ as seen in ACES (S. Longmore et al. submitted, X. Lu et al. submitted). The $25\,\mu\mathrm{m}$ emission follows the extent and orientation of the outflow.
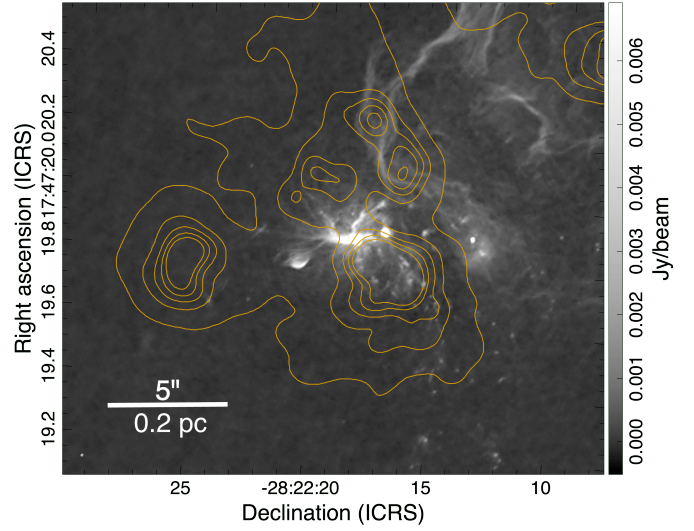
(b) 3 mm continuum ALMA from N. Budaiev et al. (2024) that was imaged with long baseline data from A. Ginsburg et al. (2018) to recover large angular scales.
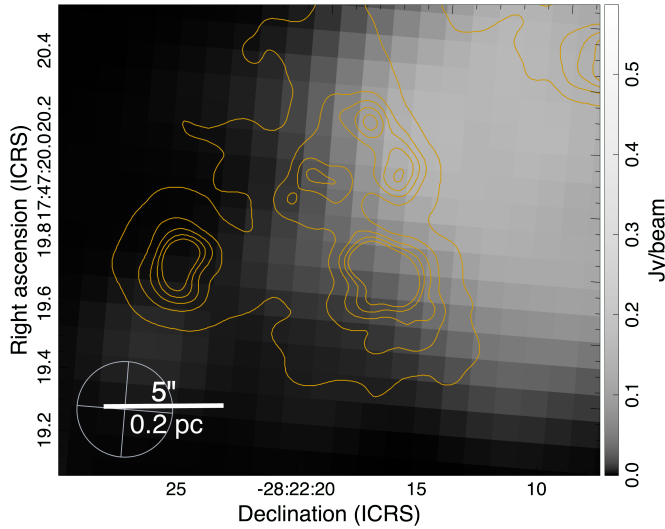
(c) 1.2 GHz continuum MeerKAT from I. Heywood et al. (2022).
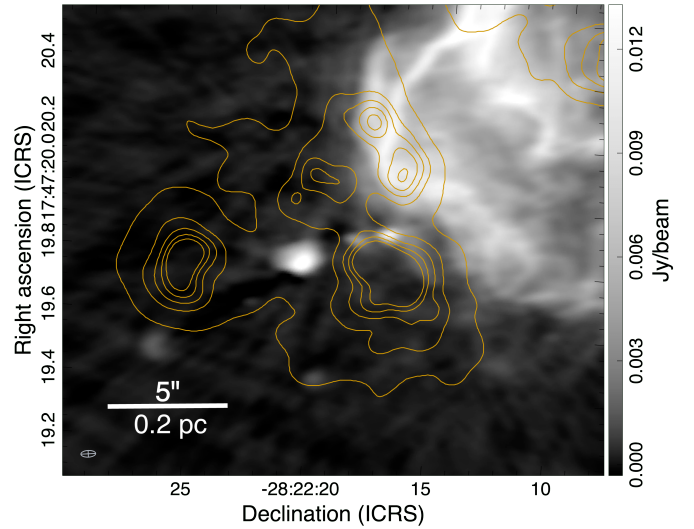
(d) 22 GHz continuum VLA from F. Meng et al. (2022).

Figure 6. A multiwavelength overview of the Sgr B2 N region. Panel (a) shows extended emission at $25\,\mu\mathrm{m}$ escaping the dense protocluster. Some of this emission was detected with *Spitzer*, however due to the resolution and the presence of nearby H II regions, seen as purple in this image, the nature of emission was ambiguous. The yellow contours show the MIRI $25.5\,\mu\mathrm{m}$ emission from panel (a). The beam sizes of the radio observations are shown as white ellipses on the bottom left.

4.3.1. *Deficit at 12 μm*

As seen in Figure 5, the fitted SED shows a significant lack of emission at 12.8 μm. In addition, both 7.7 and 25.5 μm data points show a slight deficit. Broad silicate absorption features have been observed in UCH II regions in the massive star forming region W51A (C. L. Barbosa et al. 2016), extending into the F1280W filter bandwidth. Furthermore, Y.-L. Yang et al. (2022) reported a strong absorption feature between 10 and 13 μm associated with a known H_2O libration mode around a Class 0 protostar. This feature can extend as far as 30 μm. In combination, these absorption features might be responsible for the deficit seen in MIRI filters. Dedicated spectroscopic observations of these deeply embedded objects are needed to identify the cause of the absorption at 12.8 μm and to model the extinction curve towards the Galactic center.

Among the known H II regions, there are several that exhibit similar SED features: X, Z10.24, L13.30, Y, A2 (A. Schmiedeke et al. 2016). However, their analysis is impeded by proximity to other sources, complex morphology, saturation in MIRI filters, or lack of 4 μm NIRCam detections. These compact H II regions can serve as future JWST spectroscopy targets to investigate the shape of the extinction curve in the Galactic center.

4.3.2. *JWST is able to detect UCH II regions missed by radio observations*

We use the presence of Brα emission, polycyclic aromatic hydrocarbon (PAH) emission, and the presence of warm dust to identify H II region candidates. We identify 13 previously missed sources that exhibit all three features; we designate such sources as H II region candidates. Figure 7 shows the spatial distribution of VLA-detected H II regions (A. Schmiedeke et al. 2016; F. Meng et al. 2022) and the H II region candidates revealed with JWST.

There are two types of H II region candidates observed in the JWST data: extended and near-unresolved. Comparing with the MeerKAT 1.2 GHz data, we find that some of the extended, VLA-missed H II regions are detected. However, others are located in regions of extended synchrotron emission, which obscures them from clear identification. We attribute the VLA non-detections to a lack of surface-brightness sensitivity required for the very diffuse H II regions.

The more compact H II regions are too small and too close to extended emission to be identified in MeerKAT observations. We inspect the 22 GHz data from F. Meng et al. (2022) and identify that these new H II candidates are either located in the regions significantly impacted by imaging artifacts or their 22 GHz flux is just below the detection detection threshold.

Both unresolved and slightly extended H II region candidates in the JWST data exhibit excess in F480M data. We attribute this to the radiation leaking from the UCH II region and heating up the surrounding dust, thus revealing it in our infrared observations.

Despite the numerous multiwavelength and multiscale investigations of Sgr B2 cloud, there are still new forming stars being discovered, including massive ones. The high density appears to obscure some of the recent star formation. Thus, we are still likely underestimating the star formation rate in the region and possibly the whole CMZ.

4.4. *ALMA-detected YSOs are not seen with JWST*

We cross-match the protostellar cores seen in ALMA millimeter data (A. Ginsburg et al. 2018; N. Budaiev et al. 2024, M. Daley 2026, in preparation) with the JWST NIRCam catalog. We augment the search with a by-eye inspection of the locations of the ALMA-detected YSOs. The high stellar density results in line-of-sight, by chance matches with ALMA data. An ALMA detection of a YSO requires the presence of significant amount of dust and, thus, such objects should exhibit strong reddening. To remove chance line-of-sight matches, we exclude spatial matches without 4.8 μm excess. Out of over 700 protostellar cores, only three plausible matches remain, all of which are in Sgr B2 DS. One of the three sources exhibits little CO ice absorption. This same object is the only one of the three to have a 12.8 μm detection, in line with the discussion in Section 4.3.1. The offset between the peak of the 1 mm continuum emission and long-wavelength NIRCam filters is inconsistent between the three sources, ranging between 800 and 2000 au, much larger than the astrometric accuracy ∼ 100au. Such a discrepancy in the separation indicates that if we are detecting the same object, ALMA and JWST may be seeing different parts of the YSO. The two objects that do exhibit CO ice absorption are located in the vicinity of several other ALMA-detected YSOs and have several outflow detections nearby. We highlight these two locations further in the following section, as they exhibit extended emission in JWST.

To estimate the required extinction to obscure the vast majority of the ALMA-detected protostellar cores, we use two approaches: extinction of the central stellar object and extinction of the surrounding hot dust.

We select the brightest ALMA-detected source from the Sgr B2 N and M sample that is not affected by saturation or extended emission in the F480M filter: source 168 in the 3 mm catalog from N. Budaiev et al. (2024).
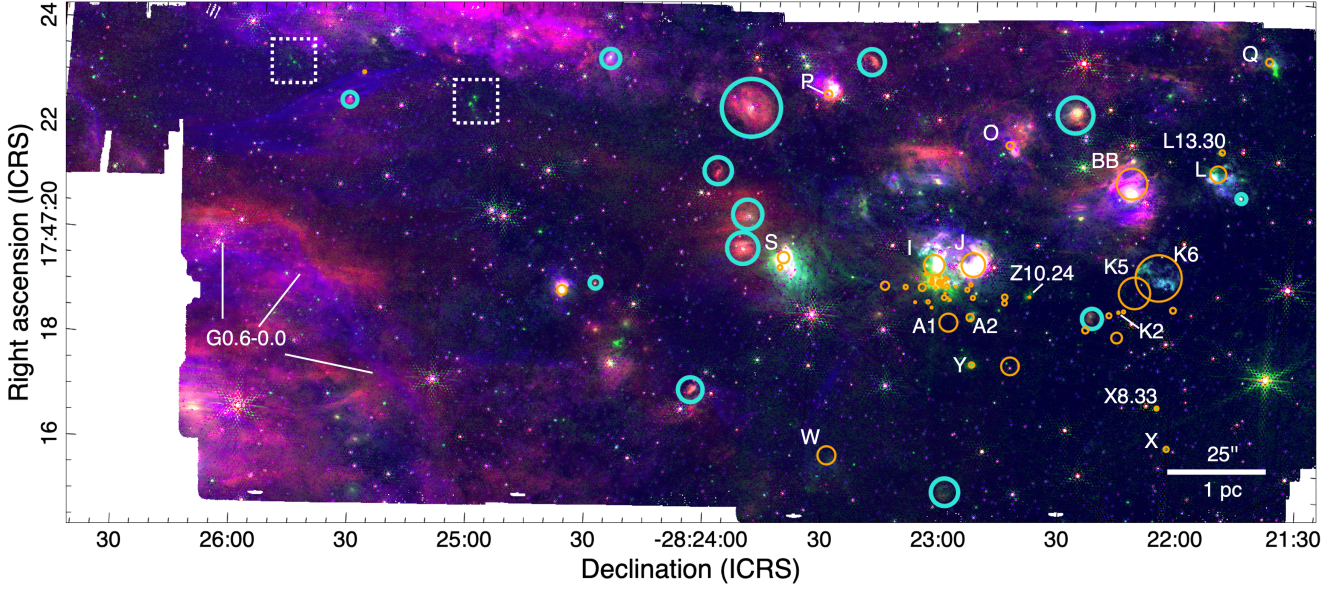
Figure 7. A tricolor NIRCam and MIRI image showing the locations of known H II regions with orange circles and new candidate H II regions detected with JWST with cyan circles. PAH emission captured in F770W is shown in red, the contribution from hot dust is shown in green (F480M−[F410M−F405N]), and the Brα recombination line is shown in blue. There are 16 H II region candidates with varying sizes: the unresolved ones are optically thick in the cm regime and thus obscured in VLA observations, while the extended ones are too diffuse. Several of the extended H II region candidates are detected with MeerKAT, but cannot be easily identified due to confusion. The white dotted squares show the locations of zoom-ins in Figure 8.

The source is marginally resolved at 1 mm with ~ 500 au resolution and has a spectral index of 1.87 ± 0.03 between 1 and 3 mm, indicating optically thick dust. The 22 GHz upper limit measurement is more than an order of magnitude below an extrapolated emission with a slope of 2. The 22 GHz non-detection suggest a lack of free-free emission and that the dust becomes optically thin between 3 mm and 1.3 cm. Assuming a 100% beam-filling factor of the $r = 350$ au beam at 3 mm, the observed radio emission requires $T_d = 170$ K. Following the SED-modeling from the previous subsection and assuming no free-free and stellar contributions, the non-detections at 4.8 and 7.7 μm require an extinction of $A_V > 200$. The majority of the ALMA-detected protostellar cores are located in N(H$_2$)$> 5 \times 10^{23}$ cm^{-2} (A. Ginsburg et al. 2018), the lack of overlap is not surprising.

Now, we assume a more evolved, Stage II/III YSO with a mass of $M = 8\,\mathrm{M}_\odot$, a higher-end mass of a star that is not producing an H II region. With $M_V \sim -1$, and

$$m_0 = M + 5\log_{10}(d/10\,\mathrm{pc}),$$

the apparent magnitude is $m_0 = 13.6$. The F480M observations are able to detect objects down to 21 mag. Converting $A_{4.8} = 7.4$ to extinction in V band assuming the J. E. Chiar & A. G. G. M. Tielens (2006) extinction law results in $A_V \sim 100$, even lower than the extinction required for the hot dust.

4.5. *JWST detects hot dust near YSOs*

We observe an apparent NIRCam long wavelength excess in some parts of Sgr B2 DS associated with early stages of star formation. Figure 8 shows the F480M excess next to SiO outflows in two locations in Sgr B2 DS. The locations of the two cutouts within the cloud are shown in Figure 7 as white dotted squares. Based on the close spatial association with regions with known outflows and YSOs we assume that this emission is the product of the active star formation. Considering the linearity of the features, we hypothesize that NIRCam emission is coming from the hot dust around the outflow cavities.

Similar objects with F480M excess, usually unresolved, are found throughout the cloud, but they are not distributed uniformly. Some of these sources are present in locations with no known star-forming activities. One explanation is that as the YSOs evolve, they move outwards within the cloud in a manner reminiscent of the observed distribution of YSOs in Orion. Alternatively, it is possible that these (some or all) are very reddened stars. NIRCam and MIRI SED fitting will distinguish between the two scenarios.
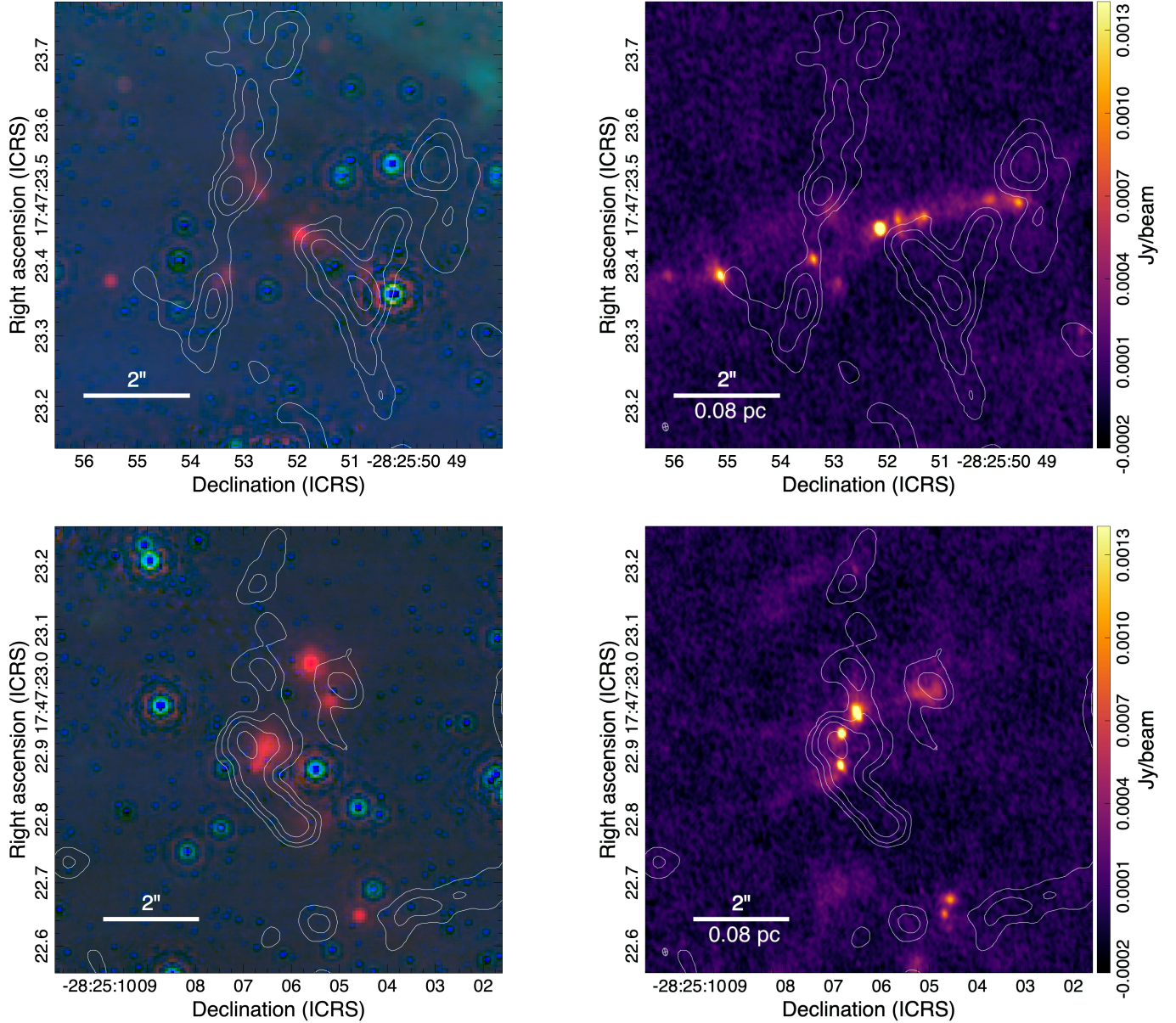
Figure 8. Left column: two selected locations that show $4.8\,\mu m$ excess that spatially overlaps with sites of star formation activity seen with ALMA. The NIRCam tricolor image has the same colors as Figure 3. The relative positions of the zoom-ins is shown in Figure 7 as white dotted squares. SiO integrated intensity map is shown with white contours indicating the locations of shocked gas produced by outflows. The emission in F480M is slightly extended, indicating that it might be emitted by hot dust. Right column: same locations, but as seen at 1 mm continuum. The ALMA continuum does not exactly match the locations of emission in JWST. This suggests that JWST is detecting more diffuse, hot dust that is optically thin at mm wavelengths, while ALMA is detecting the more dense, earlier stages of star formation in the same region that are too extincted to be detected in infrared light.

4.6. *Cloud morphology*

4.6.1. *Star formation asymmetry seen in ALMA and JWST*

Over the years of radio observations of Sgr B2, it has become apparent that the majority of the star formation in the cloud is happening towards its western side (downwards in the figures) relative to the central pro-

toclusters (e.g. A. Schmiedeke et al. 2016; A. Ginsburg et al. 2018; F. Meng et al. 2022). Studies of protostellar cores and H II regions, as well as high-resolution and high-sensitivity follow-ups show that there is ongoing star formation in the Sgr B2 N, M, and S protoclusters with "chains" of YSOs to one side and an absence of dusty cores on the other side. Figure 10 shows that the number of radio-detected YSOs and H II regions declines

slowly in one direction, while forming a sharp edge in the other direction.

JWST observations paint a different picture: most of the recently formed stars are located opposite to those seen in ALMA. The protoclusters are only barely peeking through or are detected indirectly in case of Sgr B2 N, as discussed in Section 4.2. Figure 7 further highlights that the ionized and heated gas from the recently formed stars is preferentially detected on the eastern side of the cloud. The apparent anti-correlation between mm and infrared emission can be explained with a density asymmetry in the cloud: the low-density, eastern side of the cloud does not have sufficient mass to form new dusty YSOs, and the recently formed stars illuminate the diffuse medium that is not dense enough to be detected in radio observations. On the other hand, the western, dense side of the cloud has many accreting, dusty YSOs and is completely extincted in infrared wavelengths. The origin of this type of cloud morphology is uncertain. It is also unclear whether the young stars in the eastern side of the cloud formed there and eventually cleared out the surrounding material or if they formed in the western side of the cloud and moved eastward over time.

We also note that the YSO "chains" and mm continuum filamentary structures seen outside of Sgr B2 N, M, and S in the western side of the cloud (N. Budaiev et al. 2024) are preferentially oriented in the east-west direction. Such an orientation may be indicative of either the star-forming objects moving through the dense cloud or the dense surrounding material passing through the region of ongoing star formation.

4.6.2. *Sgr B2 has a sharp edge*

We observe evidence of the sharp eastern edge of the cloud in Sgr B2 DS (see the upper left side of Figures 3, 7, 9, and 10). The extended background becomes rapidly extincted by the dense cloud as we move into Sgr B2 DS. To our knowledge, this is the sharpest cloud edge that JWST revealed in a molecular cloud. The observed cloud edge in Sgr B2 DS is consistent with the edge of SiO J=2-1 cavity D reported by J. Armijos-Abendaño et al. (2020). The nature this sharp edge, reminiscent of ionization fronts in nebulae, is unclear.

4.6.3. *Extended flocculence in Sgr B2 DS*

We observe extended $25\,\mu m$ emission in part of Sgr B2 DS. The emission is flocculent, with identifiable local peaks and missing patches as seen in Figure 9. Parts of the emitting region are visible in F1280W and F770, however the emission is extremely faint and undistinguishable among other large-scale features. Interestingly, the region also emits Brα recombination line.

The patchy emission begins near the edge of the Sgr B2 DS region and extends for $30''$, forming a circular shape. The right side of the region is dimmer, either due to lack of the underlying emission, or because of foreground material obscuring the emission. We do not know what drives this unique morphology. While the rough symmetry seen in Figure 9 (right) hints at a central feedback-driven mechanism, there is no obvious configuration that would produce such a flocculent morphology.

4.6.4. *Is Sgr B2 behind Sgr B1?*

The NIRCam footprint includes an extended H II region G0.6-0.0, which is part of the ridge of features connecting Sgr B2 and Sgr B1. Typically, Sgr B2 is placed in front of Sgr B1 and the surrounding features, including G0.6-0.0, relative to Earth (D. M. Mehringer et al. 1992, 1993; A. I. Harris et al. 2021). Furthermore, the widely adopted orbital configuration over the past decade is such that the younger cloud, Sgr B2, is located in the front, with G0.6-0.0 and the older Sgr B1 cloud further along the back-side of the orbit (J. M. D. Kruijssen et al. 2015; A. T. Barnes et al. 2017). However, the NIRCam observations suggest that G0.6-0.0 could be located in front of Sgr B2. As discussed in Section 4.6.2, the dense star forming ridge Sgr B2 DS is seen as a dark patch lit up by the extended background emission: a clear and sharp edge of the dusty cloud can be seen absorbing the background recombination line emission and glowing dust. However, where Sgr B2 DS meets with the footprint of G0.6-0.0 H II region in the bottom left of the images, no such sharp features are seen. Instead, the diffuse emission fades, not showing any signs of sharp increase in extinction. Critically, the emission from PAHs seen in F770W extends even further beyond the Brα emission as seen in Figure 10. The thermal emission in Sgr B2 DS detected in A. Ginsburg et al. (2018) and described in F. Meng et al. (2019) extends to the edge of the recombination line features from G0.6-0.0 and partially overlaps with the location of the PAH emission. The lack of absorption features strongly suggests that G0.6-0.0 is not extincted by Sgr B2 DS.

The most likely remaining explanation is that G0.6-0.0 H II region is located in front of Sgr B2 DS. The recombination line-based extinction to parts of G0.6-0.0 is $A_V = 50$, indicating that the H II region is not located at the "surface" of the CMZ either. Such spatial configuration is consistent with the bow-shock model of Sgr B cloud complex proposed by Y. Sofue (2024). However, no large-scale structures validating the presence of a bow shock are present, likely due to the compact spatial coverage. It is not clear whether the whole Sgr B1
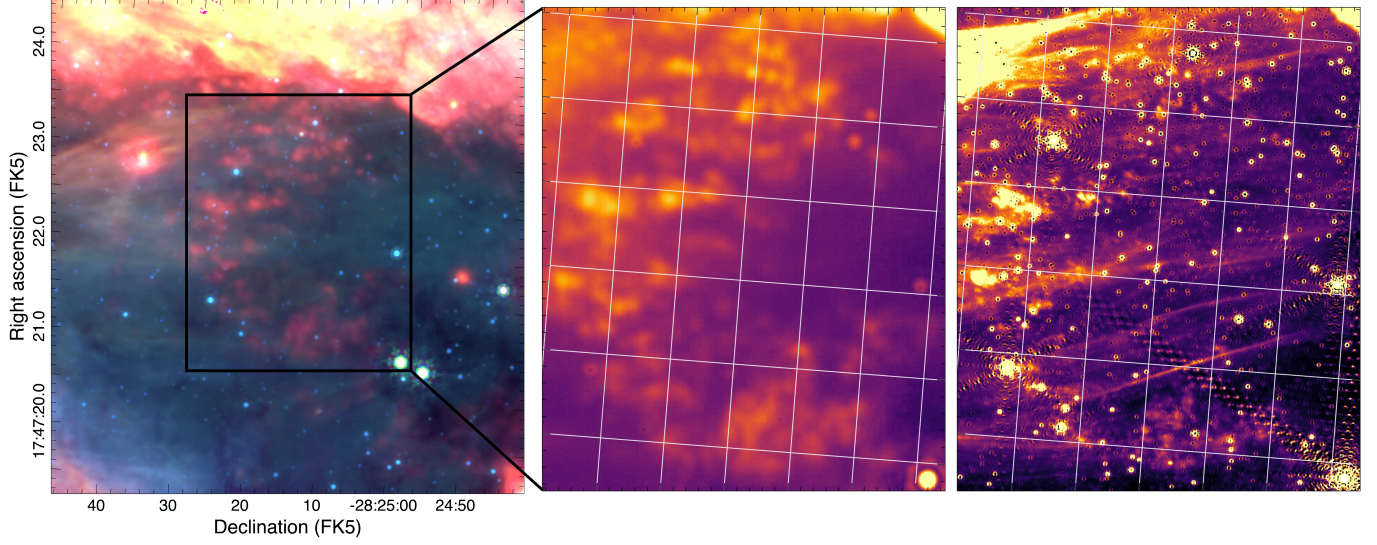
Figure 9. Left: MIRI tricolor image covering part of Sgr B2 DS that shows extended flocculent emission. The structure is only apparent at $25\,\mu$m due to other large-scale emission at other wavelengths. Middle: F2550W-only view of the emission. The feature appears to have a spherical shape with dense material extincting some of the emission on the right hand side. The cause for this flocculent structure as well as the source of the emission remain unclear. Right: same region as the middle panel, but as seen in Brα.
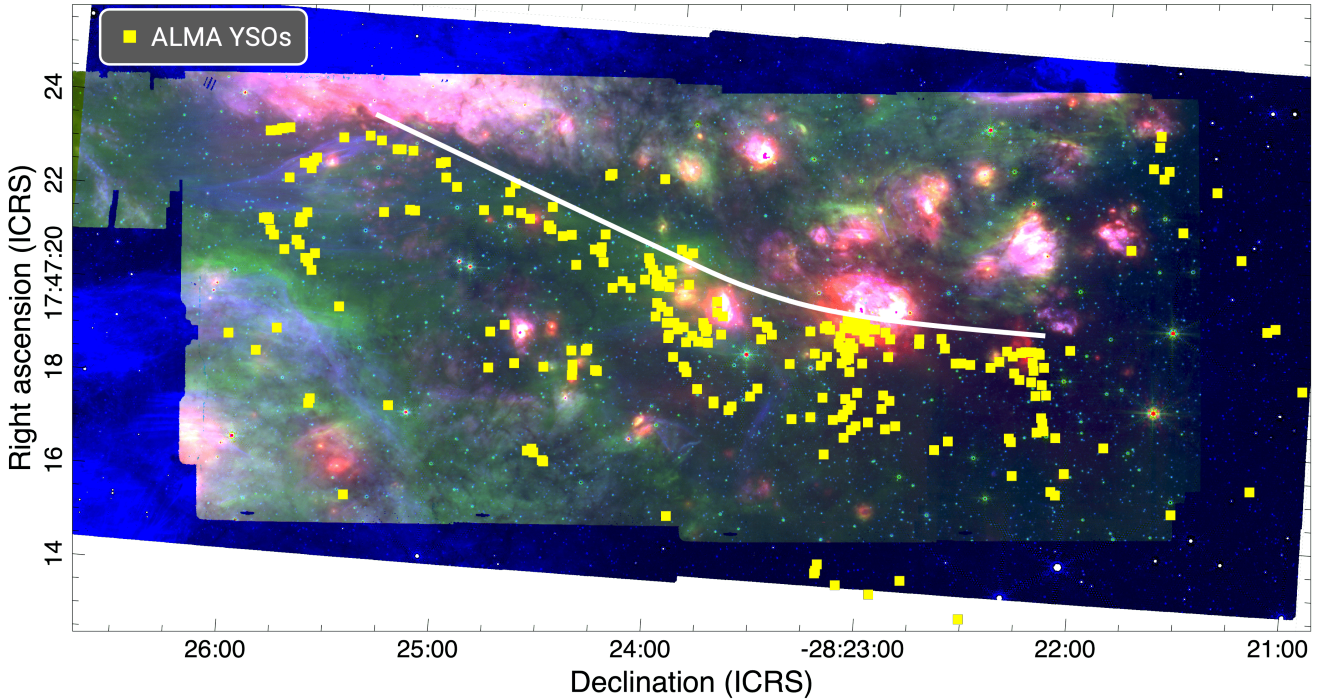
Figure 10. Star formation asymmetry in Sgr B2: ALMA-detected YSOs are detected on one side of the cloud (A. Ginsburg et al. 2018), while the JWST reveals recently formed stars on the other side of the cloud. The white line separates the two distinct regions, highlighting the sharp transition. F2550W is shown in red, F770W (PAHs) is shown in green, and Brα recombination line is shown in blue.

complex is located in front of Sgr B2 or only the G0.6-0.0 H II region is. Almost the entirety of the CMZ is populated with bright, wispy thermal and synchrotron emission seen with radio telescopes. IR observations of recombination lines provide a way to identify the heavily extincted regions.

4.7. *Preliminary CCDs*

We use the preliminary NIRCam and MIRI stellar catalogs to produce color-color diagrams (CCDs) and color-magnitude diagrams. As discussed in Section 2.2, source extraction tools (e.g. `crowdsource`, `daophot`) struggle with extremely crowded fields towards the Galactic center. The images are further complicated by the bright extended emission and several extremely bright stars (H mag < 9) and thus extended PSF artifacts. The resulting catalog is contaminated with false positives, and the extracted fluxes are sometimes contaminated by the surrounding emission. We use the version of the catalog where any detection satisfies the filtering criteria in all filters where it is detected.

As expected for a dense molecular cloud, a significant amount of ice is present. The top row of Figure 11 highlights H_2O ice absorption in F300M and CO ice absorption in F466N. In panel (a), the foreground stars follow the extinction vector up to $A_V \approx 17$ and then begin being significantly affected by the H_2O absorption. Panel (b) shows a similar effect from the CO ice. Comparing the two ices, it appears that the H_2O ice has a stronger absorption effect than the CO ice. CCDs with the F360M filter show slight lack of $3.6\,\mu m$ emission at high extinction. We attribute this to the broad $3\,\mu m$ H_2O or methanol absorption affecting the F360M filter. Panel (c) shows that [F182M]−[F212N] and [F212N]−[F410M] generally line up with the extinction vector with a slight contribution from CO ice at the edges of the F410M filter. The two foreground spiral arms are identifiable via the two groups of sources on the lower-left tail of the distribution. At longer wavelengths, the red clump stars become more apparent: in panel (d) the red clump stars show up as high density of sources at $M_{7.7\,\mu m} = 18$. At the longer wavelengths we are able to probe larger extinctions reaching deeper into the cloud down to several hundred magnitudes in V band.

5. CONCLUSIONS

We presented JWST's NIRCam and MIRI first view of the most vigorously star forming cloud in the CMZ, Sagittarius B2.

- The constructed SEDs of UCH II regions show significant deficit at $12.8\,\mu m$. The broadening of the $10\,\mu m$ silicate absorption feature in a dense environment as well as a strong water libration feature are the likely causes.

- MIRI revealed infrared radiation escaping the dense protocluster Sgr B2 N following the path of a large-scale outflow. The presence of extended $25\,\mu m$ emission suggests that infrared photons do not get trapped within dense clusters.

- Despite extensive radio regime studies of the region, we detect over a dozen new H II region candidates in the cloud. The high sensitivity of our observations allowed for detection of diffuse H II regions.

- ALMA-detected YSOs are too deeply embedded to be detected with JWST. However, JWST appears to detect hot dust around the outflow cavities.

- The cloud shows very structured morphology. The earliest stages of star formation are present in the western side of the cloud as seen with ALMA, while JWST detects recent star formation in the eastern, less dense part of the cloud. The Sgr B2 DS region is being backlit by extended recombination line emission showing the sharp cloud edge on one side. G0.6-0.0, which is an H II region thought to be associated with the Sgr B1 cloud, appears to be in front of Sgr B2 DS. This is contrary to the typical view of the relative location of the two clouds.

(a) A CCD showing a significant absorption in F300M filter from H_2O ice.

(b) A CCD showing a significant absorption in F466N filter from CO ice.

(c) A CCD showing that the observed stellar extinction generally aligns with the extinction model from J. E. Chiar & A. G. G. M. Tielens (2006).

(d) A CMD showing high extinction observed with longer wavelengths. The red clump stars appear a high density group on the plot. The outline arrow shows projection of the extinction vector onto the x-axis.

Figure 11. Color-color and color-magnitude diagrams showing the general features seen in the cloud. Significant amount of H_2O and CO ice is present in the cloud.

AUTHOR CONTRIBUTIONS

N.B. acquired the observations, led the analysis, writing, and interpretation. A.G. acquired the observations, oversaw the project progress, and contributed to the interpretation and writing. A.T.B. and D.J. were instrumental in acquiring the observations and contributed to the interpretation. T.Y. contributed to the interpretation. C.B., A.B., X.L., E.M., and D.L.W. were instrumental in acquiring the observations.

Facilities: JWST, ALMA

APPENDIX

A. PERSISTENCE IN MIRI

The F2550W data show depressed central pixels for some of the sources. This is especially apparent in the dimmer point sources. The depressed pixels are present in the raw, uncalibrated files across all five dithers. This is indicative of persistence caused by the prior observations with the F1280W filter. This is further evidenced by the presence of depressed pixels in the combined image at the locations where the bright star was on the detector at each of the dithers. Points sources above ~ 0.001 Jy in the F1280W filter are affected by persistence. The effect is especially amplified in the sources that are bright in F1280W while being dimmer in F2550W. Both F2550W and F1280W filters have several regions with slew persistence, another typical artifact for fields with bright stars.

D. Dicken et al. (2024) reports $< 0.01\%$ flux contribution from persistence after 15 minutes of the saturating observations. At the same time, they report an instance of slew persistence that lasted much longer than other examples and modeling, and no cause was identified (PID 2736). While the commissioning investigations of persistence did not include the evaluation of the impact on the ramp fitting process, the persistence-induced error is usually estimated to be below 1%. However, we observe that the central few pixels are dimmed by up to 5% relative to the surrounding pixels.

Currently, no persistence mitigation tools are implemented in the STScI's pipeline for MIRI observations. Nevertheless, it is likely possible to use the depressed pixels at the locations without stellar contribution to model the persistence and apply the correction to the affected pixels.

B. POSSIBLE PLANETARY NEBULA DETECTION

We detect two objects that appear to be planetary nebulae based on their morphology and observed line emission. Figure 12 shows one of such objects as seen in NIRCam and MIRI filters. The object shows uniform and spherically symmetrical emission in both Paα and Brα recombination lines. Using the line ratio we determine the extinction to this object of $\sim A_V = 40$. Considering that the extinction to the Galactic center of $A_V \approx 17$, the object is possibly located far behind the Galactic center, but in the plane-of-sky region without dense gas. The second such object has $A_V = 50$. At the edges of recombination line emission bright H_2 emission is seen, evidence of the UV-excitation typical for PNe. The one source covered by the MIRI mosaic is detected at 12 and $25\,\mu m$. The lack of detection in F770W indicates the absence of PAH emission, which is also in line with the PNe conjecture. Both objects have no detections in the radio regime, which is expected due to low surface brightness. For both objects, no central star is detected. Considering the low extinction, it is likely that the central object is a white dwarf.

REFERENCES

Armijos-Abendaño, J., Banda-Barragán, W. E., Martín-Pintado, J., et al. 2020, Monthly Notices of the Royal Astronomical Society, 499, 4918, doi: 10.1093/mnras/staa3119

Armitage, P. J. 2000, Suppression of giant planet formation in stellar clusters, arXiv, doi: 10.48550/arXiv.astro-ph/0007044

Astropy Collaboration, Robitaille, T. P., Tollerud, E. J., et al. 2013, Astronomy and Astrophysics, 558, A33, doi: 10.1051/0004-6361/201322068

Astropy Collaboration, Price-Whelan, A. M., Sipőcz, B. M., et al. 2018, The Astronomical Journal, 156, 123, doi: 10.3847/1538-3881/aabc4f

Astropy Collaboration, Price-Whelan, A. M., Lim, P. L., et al. 2022, The Astrophysical Journal, 935, 167, doi: 10.3847/1538-4357/ac7c74

Barbosa, C. L., Blum, R. D., Damineli, A., Conti, P. S., & Gusmão, D. M. 2016, The Astrophysical Journal, 825, 54, doi: 10.3847/0004-637X/825/1/54

Barnes, A. T., Longmore, S. N., Battersby, C., et al. 2017, Monthly Notices of the Royal Astronomical Society, 469, 2263, doi: 10.1093/mnras/stx941

Budaiev, N., Ginsburg, A., Goddi, C., et al. 2025, The Astrophysical Journal, 989, 52, doi: 10.3847/1538-4357/adea3b
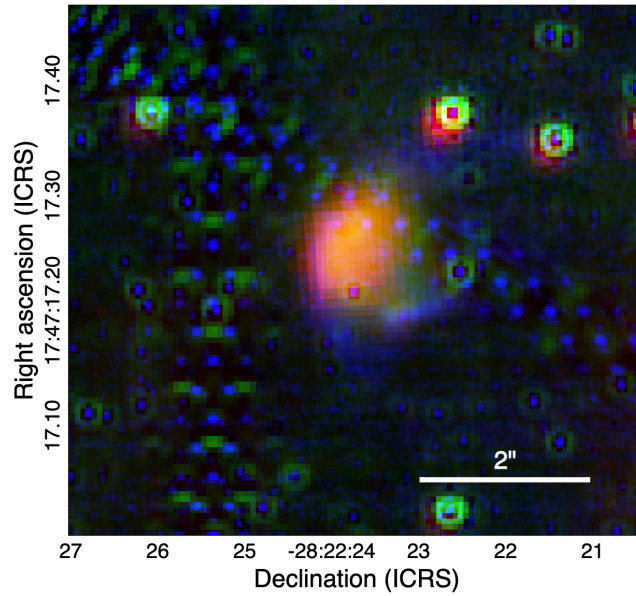
18

Figure 12. A candidate planetary nebula shown in a tricolor image with F1280W in red, Brα in green, and H₂ in blue. The extinction based on the recombination line ratio is $A_V = 40$.

Budaiev, N., Ginsburg, A., Jeff, D., et al. 2024, The Astrophysical Journal, 961, 4, doi: 10.3847/1538-4357/ad0383

Chiar, J. E., & Tielens, A. G. G. M. 2006, The Astrophysical Journal, 637, 774, doi: 10.1086/498406

Crowe, S., Fedriani, R., Tan, J. C., et al. 2025, The Astrophysical Journal, 983, 19, doi: 10.3847/1538-4357/ad8889

Daffern-Powell, E. C., & Parker, R. J. 2022, Monthly Notices of the Royal Astronomical Society, 517, 2103, doi: 10.1093/mnras/stac2797

Dicken, D., Marín, M. G., Shivaei, I., et al. 2024, Astronomy and Astrophysics, 689, A5, doi: 10.1051/0004-6361/202449451

Draine, B. T. 2011, Physics of the Interstellar and Intergalactic Medium. https://ui.adsabs.harvard.edu/abs/2011piim.book.....D

Duchêne, G., Lacour, S., Moraux, E., Goodwin, S., & Bouvier, J. 2018, Monthly Notices of the Royal Astronomical Society, doi: 10.1093/mnras/sty1180

Ginsburg, A., & Kruijssen, J. M. D. 2018, The Astrophysical Journal Letters, 864, L17, doi: 10.3847/2041-8213/aada89

Ginsburg, A., Bally, J., Barnes, A., et al. 2018, The Astrophysical Journal, 853, 171, doi: 10.3847/1538-4357/aaa6d4

Ginsburg, A., Barnes, A. T., Battersby, C. D., et al. 2023, The Astrophysical Journal, 959, 36, doi: 10.3847/1538-4357/acfc34

Gordon, K. D., Clayton, G. C., Decleir, M., et al. 2023, The Astrophysical Journal, 950, 86, doi: 10.3847/1538-4357/accb59

GRAVITY Collaboration, Abuter, R., Aimar, N., et al. 2022, Astronomy & Astrophysics, 657, L12, doi: 10.1051/0004-6361/202142465

Harris, A. I., Güsten, R., Requena-Torres, M. A., et al. 2021, The Astrophysical Journal, 921, 33, doi: 10.3847/1538-4357/ac1863

Henshaw, J. D., Barnes, A. T., Battersby, C., et al. 2022, Star Formation in the Central Molecular Zone of the Milky Way, arXiv, doi: 10.48550/ARXIV.2203.11223

Heywood, I., Rammala, I., Camilo, F., et al. 2022, The Astrophysical Journal, 925, 165, doi: 10.3847/1538-4357/ac449a

Higuchi, A. E., Hasegawa, T., Saigo, K., Sanhueza, P., & Chibueze, J. O. 2015, The Astrophysical Journal, 815, 106, doi: 10.1088/0004-637X/815/2/106

Hosek, M. W., Lu, J. R., Anderson, J., et al. 2019, The Astrophysical Journal, 870, 44, doi: 10.3847/1538-4357/aaef90

Jeff, D., Ginsburg, A., Bulatek, A., et al. 2024, The Astrophysical Journal, 962, 48, doi: 10.3847/1538-4357/ad1507

Kruijssen, J. M. D. 2012, Monthly Notices of the Royal Astronomical Society, 426, 3008, doi: 10.1111/j.1365-2966.2012.21923.x

Kruijssen, J. M. D., Dale, J. E., & Longmore, S. N. 2015, Monthly Notices of the Royal Astronomical Society, 447, 1059, doi: 10.1093/mnras/stu2526

Kruijssen, J. M. D., & Longmore, S. N. 2013, Monthly
Notices of the Royal Astronomical Society, 435, 2598,
doi: 10.1093/mnras/stt1634

Krumholz, M. R., & Matzner, C. D. 2009, The
Astrophysical Journal, 703, 1352,
doi: 10.1088/0004-637X/703/2/1352

Longmore, S. N., Bally, J., Testi, L., et al. 2013, Monthly
Notices of the Royal Astronomical Society, 429, 987,
doi: 10.1093/mnras/sts376

Madau, P., & Dickinson, M. 2014, Annual Review of
Astronomy and Astrophysics, 52, 415,
doi: 10.1146/annurev-astro-081811-125615

Mehringer, D. M., Palmer, P., Goss, W. M., & Yusef-Zadeh,
F. 1993, The Astrophysical Journal, 412, 684,
doi: 10.1086/172954

Mehringer, D. M., Yusef-Zadeh, F., Palmer, P., & Goss,
W. M. 1992, The Astrophysical Journal, 401, 168,
doi: 10.1086/172050

Meng, F., Sánchez-Monge, Á., Schilke, P., et al. 2019,
Astronomy and Astrophysics, 630, A73,
doi: 10.1051/0004-6361/201935920

Meng, F., Sánchez-Monge, Á., Schilke, P., et al. 2022,
Astronomy and Astrophysics, 666, A31,
doi: 10.1051/0004-6361/202243674

Menon, S. H., Federrath, C., & Krumholz, M. R. 2022,
Monthly Notices of the Royal Astronomical Society, 517,
1313, doi: 10.1093/mnras/stac2702

Menon, S. H., Federrath, C., & Krumholz, M. R. 2023,
Monthly Notices of the Royal Astronomical Society, 521,
5160, doi: 10.1093/mnras/stad856

Murray, N., Quataert, E., & Thompson, T. A. 2010, The
Astrophysical Journal, 709, 191,
doi: 10.1088/0004-637X/709/1/191

Nogueras-Lara, F., Schödel, R., Najarro, F., et al. 2019,
Astronomy and Astrophysics, 630, L3,
doi: 10.1051/0004-6361/201936322

Nogueras-Lara, F., Schödel, R., & Neumayer, N. 2021,
Astronomy and Astrophysics, 653, A133,
doi: 10.1051/0004-6361/202140996

Perrin, M. D., Sivaramakrishnan, A., Lajoie, C.-P., et al.
2014, in Society of Photo-Optical Instrumentation
Engineers (SPIE) Conference Series, Vol. 9143, Space
Telescopes and Instrumentation 2014: Optical, Infrared,
and Millimeter Wave, ed. J. M. Oschmann, Jr.,
M. Clampin, G. G. Fazio, & H. A. MacEwen, 91433X,
doi: 10.1117/12.2056689

Perrin, M. D., Soummer, R., Elliott, E. M., Lallo, M. D., &
Sivaramakrishnan, A. 2012, in Society of Photo-Optical
Instrumentation Engineers (SPIE) Conference Series,
Vol. 8442, Space Telescopes and Instrumentation 2012:
Optical, Infrared, and Millimeter Wave, ed. M. C.
Clampin, G. G. Fazio, H. A. MacEwen, & J. M.
Oschmann, Jr., 84423D, doi: 10.1117/12.925230

Pfeffer, J., Kruijssen, J. M. D., Crain, R. A., & Bastian, N.
2018, Monthly Notices of the Royal Astronomical
Society, 475, 4309, doi: 10.1093/mnras/stx3124

Rybicki, G. B., & Lightman, A. P. 1979, Radiative
processes in astrophysics.
https://ui.adsabs.harvard.edu/abs/1979rpa..book.....R

Schmiedeke, A., Schilke, P., Möller, T., et al. 2016,
Astronomy & Astrophysics, 588, A143,
doi: 10.1051/0004-6361/201527311

Sofue, Y. 2024, Monthly Notices of the Royal Astronomical
Society, 532, 4187, doi: 10.1093/mnras/stae1724

Thompson, T. A., Quataert, E., & Murray, N. 2005, The
Astrophysical Journal, 630, 167, doi: 10.1086/431923

Walker, D. L., Longmore, S. N., Bastian, N., et al. 2016,
Monthly Notices of the Royal Astronomical Society, 457,
4536, doi: 10.1093/mnras/stw313

Yang, Y.-L., Green, J. D., Pontoppidan, K. M., et al. 2022,
The Astrophysical Journal, 941, L13,
doi: 10.3847/2041-8213/aca289